AEROSPACE INFLUENCE ON HEAT TRANSFER ANALYSIS ON HYBRID DUSTY NANOFLUID LOADED WITH COBALT-MWCNT NANOPARTICLES OVER A HEATED STRETCHING SHEET

Gunisetty RAMASEKHAR[*], **Shaik JAKEER**[**], **Seethi Reddy Reddisekhar REDDY**[***], **P. Vijay KUMAR**[****], **P. DURGAPRASAD**[****]

[*]Department of Mathematics, Rajeev Gandhi Memorial College of Engineering and Technology (Autonomous),
Nandyal 518501, Andhra Pradesh, India
[**]School of Technology, The Apollo University, Chittoor, A.P, India-517127
[***]Department of Mathematics, Koneru Lakshmaiah Education Foundation, Bowrampet, Hyderabad-500043, India
[****]Department of Mathematics, SAS, Vellore Institute of Technology, Chennai-600127, T.N., India

gunisettyrama@gmail.com, shaik_j@apollouniversity.edu.in,
reddyshekara43@gmail.com, vijaykumar.p@vit.ac.in, durgaprasad.p@vit.ac.in

received 12 February 2025, revised 12 November 2025, accepted 17 November 2025

Abstract: Numerous creative kinds of materials with specific aeronautical uses have been developed over the last few decades. Engine oil serves several functions in an aviation engine, which involve lubrication, cooling purposes, maintenance, rust prevention, and noise lessening. The most important is lubrication. Naturally, without lubrication, all moving components would rapidly run away. This project's effort focuses on reducing expenses by increasing the useful lives of aeroplane parts, in addition to enhancing fuel economy, carrying capacity, and flying range. The significance of the heat transfer analysis on magnetohydrodynamic dusty hybrid nanofluid across a porous stretching sheet with Darcy-Forchheimer flow and thermal radiation are examined in this present study. Appropriate self-similarity conversion is used to change the PDEs into ODEs. After applying transformations, we employed the Bvp4c in the MATLAB solver for graphical purposes. This was done after doing the modifications. Graphs and tables illustrate the effect of active parameters on the fluid's ability to convey significance. The same pattern emerges with increasing values of the l parameter: the energy outline and velocity outline both show a decline. The study we conducted led us to conclude that dusty nanofluids are not as effective in transferring heat as hybrid nanofluids.

Key words: entropy generation, dusty fluid, MHD, Darcy Forchheimer flow, thermal radiation, porous medium

1. INTRODUCTION

Since the majority of industrial and naturally occurring fluids contain suspended tiny or millimeter-sized solid particles, often known as dust nanoparticles, it is very difficult to obtain a fluid that is fully free of impurities. The presence of these dust particles markedly affects the thermophysical properties of fluids, frequently improving their heat and mass transport efficiency. These two-phase systems, referred to as dusty fluids, are named for the distributed particulate matter that modifies flow and energy transport properties. The examination of dusty fluids has garnered significant interest owing to their extensive practical uses, such as in oil and gas transportation, combustion systems, nuclear reactor cooling, geothermal energy systems, and diverse aerospace and industrial operations. Comprehensive investigations have focused on the influence of dust particles on enhancing heat transfer efficiency under various flow conditions [1–4]. The seminal research in this domain originates from Saffman [5], who formulated the governing equations for the dynamics of dusty gases based on specific simplifying assumptions. He regarded the dust particle cloud as a pseudo-fluid, disregarding individual particle interactions inside the continuum model. Marble [6] susequently expanded this concept by examining the dynamic behavior of gases with fine solid particles, establishing a foundation for further research on dusty gas dynamics and hybrid nanofluids. The rising need for efficient thermal systems across diverse engineering and industrial sectors has rendered heat transfer improvement a significant area of study in recent years. Traditionally, pure fluids like water, ethylene glycol, and motor oil have served as heat transfer medium; however, their poor thermal conductivity constrains their efficacy in high-performance applications. To address this issue, researchers developed nanofluids, which consist of nanoparticles suspended in a base fluid to improve its thermal properties. The term “hybrid nanofluid” was coined to denote fluids that include two or more distinct nanoparticles concurrently distributed in a base liquid. The collective activity of these nanoparticles has synergistic effects that markedly enhance thermal conductivity, viscosity, and total energy transfer efficiency. Due to their exceptional thermophysical properties, hybrid nanofluids are employed in various technical and commercial applications, such as automotive braking fluids, solar water heating systems, refrigeration units, heat exchangers, power transformers, and microelectronic cooling systems [7, 8]. Numerous researchers have conducted comprehensive studies employing diverse hybrid nanoparticle.

The usage and conversion of solar energy are both significantly aided by thermal radiation, which serves as a key process in a variety of solar thermal systems. The majority of the solar radiation that reaches the Earth is composed of wavelengths that are visible and infrared. These wavelengths are absorbed by collector surfaces and then transformed into heat energy via the process of radiative transfer. In subsequent steps, the thermal energy that has been absorbed is transferred to working fluids, which may include water, oil, or nanofluids. These working fluids are utilized in applications such as solar water heating, power production, and thermal storage. These systems are very dependent on the absorptivity, emissivity, and conductivity of the collector materials in order to achieve their desired level of efficiency. Due to the better optical and thermal properties of nanofluids and hybrid nanofluids, the incorporation of these materials into solar collectors results in an additional enhancement of the radiative heat transfer characteristics. The inclusion of nanoparticles enables greater thermal conductivity and enhanced absorption of incoming solar radiation, which ultimately leads to increased rates of energy conversion. Furthermore, the modeling of thermal radiation, which is frequently based on the Rosseland diffusion approximation, is helpful in comprehending the radiative heat transport that occurs within the material that is being studied. The optimization of radiative heat transfer is vital for improving performance and decreasing energy losses in advanced applications such as solar towers, photovoltaic–thermal hybrid systems, and concentrated solar power plants. As a result, thermal radiation has become an essential component of current solar energy engineering [9–14].

The study of the motion and behavior of electrically conducting fluids, such as plasmas, liquid metals, and electrolytes, when they are exposed to magnetic fields is referred to as "magnetohydrodynamics" which is abbreviated as "MHD." The interaction between the electric current created by a magnetic field and a flowing conductive fluid is the basic premise of magnetic hydrodynamics (MHD). The movement of this kind of fluid through a magnetic field causes the generation of electromagnetic forces called Lorentz forces, which in turn change the fluid's pressure, temperature, and velocity. The induced current changes the existing magnetic field, which in turn affects the flow dynamics as a whole, as a result of this interaction, which forms a linked connection. Numerous fields, including geophysics, biomedical engineering, astronomy, and industrial processes, make use of MHD. Engineering applications include MHD generators, liquid metal cooling systems, and aerospace propulsion devices; astrophysical applications include explanations of solar flares, sunspots, and plasma dynamics; biomedical applications include drug targeting and controlled transport using magnetic fields; geophysical applications include explanations of Earth's magnetic field and core convection; and engineering applications include MHD generators [15–17]. An example of the strong coupling between magnetic forces and fluid motion in magnetohydrodynamic systems is the impact that a magnetic field may have on the behavior of a conductive fluid's boundary layer through electromagnetic damping or acceleration effects. Sajid et al .[18] investigated the irreversibility process and thermal energy properties of a tetra-hybrid radiative binary nanofluid, highlighting its possible uses in solar energy systems. Sakkaravarthi et al. [19] use a neural network, especially the Levenberg-Marquardt method, to investigate the entropy optimization performance of a Casson tetra-hybrid nanofluid flowing electro-magneto-hydrodynamically across a spinning disk. Hussain et al. [20] conducted an investigation on the radiative magneto–cross Eyring–Powell fluid flow with activation energy across a porous stretched wedge. They took into consideration the effects of suction/injection as well as ohmic heating. Ali et al. [21] investigated the concentration and temperature boundary layers of a Maxwell nanofluid that contained nanoparticles. They focused on the impact that thermophoretic and Brownian motion effects had on the properties of heat and mass transport [22].

The current research states that in order to comprehend complex transport phenomena in hybrid nanofluids, the simultaneous impacts of Darcy–Forchheimer porous drag and magnetohydrodynamic (MHD) flow across a stretching sheet have been studied. For the purpose of making numerical computations easier, the governing equations that describe such flows are stated as nonlinear partial differential equations (PDEs). These equations are then translated into ordinary differential equations (ODEs) by employing appropriate similarity transformations. After the equations have been converted, the Bvp4c solver in MATLAB is used to solve them so that the numerical evaluation can be accurate. A comparison of the various nanoparticle additions reveals that MWCNT nanoparticles have a rather minor influence on heat transmission. On the other hand, cobalt nanoparticles demonstrate a stronger thermal enhancement due to their superior thermal conductivity and magnetic characteristics. When it comes to aerospace thermal systems, notably aircraft engines, where components are subjected to extremely high temperatures, the significance of cobalt is especially apparent. With a melting point of around 1,495 degrees Celsius, cobalt offers exceptional resistance to high thermal stresses, allowing it to maintain its stability even in situations with temperatures that are higher than 1,400 degrees Celsius. Because of its outstanding heat tolerance, cobalt is a material that is highly sought after in aerospace applications. This underscores the significance of cobalt in improving the heat transfer efficiency of hybrid dusty nanofluids that are utilized over heated stretched surfaces.

2. MATHEMATICAL MODELING

In the presence of dusty hybrid particles, steady 2D leading Cobalt/MWCNT-engine oil nanofluid flow has been taken into the account. Flowing across a heated stretching sheet is the dusty hybrid nanofluid via a porous medium. In this model we considered the sheet is taken as along the x—axis and the flow confined to $y > 0$. Here we taken the y—axis is normal to the sheet. The movement of the heated stretching sheet taking the x—axis is uw(x). And also, an additional M field strength B0 is forced through x—axis see in (Fig. 1). Table 1 displays the straightforward results of the nanoparticles and base fluid. The arranged governing flow equations are [23–25]

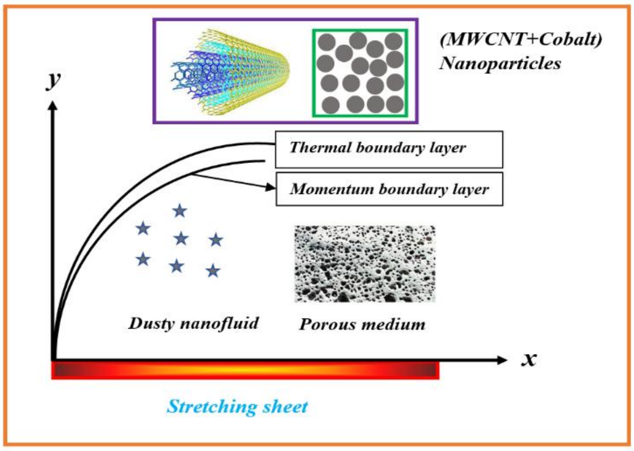

Fig. 1. Geometry of the problem

Fluid Phase:

$$\frac{\partial u}{\partial x}+\frac{\partial v}{\partial y}=0 \tag{1}$$

$$u\frac{\partial u}{\partial x}+v\frac{\partial u}{\partial y}=\frac{\mu_{hnf}}{\rho_{hnf}}\left(\frac{\partial^2 u}{\partial y^2}\right)+\frac{KN}{\rho_{hnf}}\left(\overline{u_p}-u\right)-\frac{\sigma_{hnf}B^2}{\rho_{hnf}}(u)-\frac{\upsilon_{hnf}}{k^*}(u)-\frac{C_F}{\sqrt{k}}u^2 \tag{2}$$

$$u\frac{\partial T}{\partial x}+v\frac{\partial T}{\partial y}=\frac{k_{hnf}}{(\rho c_p)_{hnf}}\left(\frac{\partial^2 T}{\partial y^2}\right)+\frac{N(c_p)_f}{\tau_T(\rho c_p)_{hnf}}\left(\overline{T_p}-T\right)+\frac{N}{\tau_v(\rho c_p)_{hnf}}\left(\overline{u_p}-u\right)^2+\frac{16\sigma^*T_\infty^3}{3k^*(\rho c_p)_{hnf}}\left(\frac{\partial^2 T}{\partial y^2}\right)+\frac{\sigma_{hnf}B^2}{(\rho c_p)_{hnf}}u^2 \tag{3}$$

Dusty Phase:

$$\frac{\partial \overline{u_p}}{\partial x}+\frac{\partial \overline{v_p}}{\partial y}=0, \tag{4}$$

$$\overline{u_p}\frac{\partial \overline{u_p}}{\partial x}+\overline{v_p}\frac{\partial \overline{u_p}}{\partial y}=\frac{K}{m}\left(u-\overline{u_p}\right), \tag{5}$$

$$N_1 r_m\left(\overline{u_p}\frac{\partial \overline{T_p}}{\partial x}+\overline{v_p}\frac{\partial \overline{T_p}}{\partial y}\right)=\frac{N_1(c_p)_f}{\tau_T}\left(T-\overline{T_p}\right). \tag{6}$$

The carrier is a hybrid nanofluid flowing over a stretching surface at $y=0$ with $u_w(x)=rx$. A monodisperse dusty (particle) phase is suspended in the carrier; both phases interact through linear Stokes-type drag (momentum exchange) and temperature relaxation (thermal exchange). The flow is steady, laminar, and two-dimensional in the boundary-layer approximation. The governing continuity, momentum, and energy equations for the fluid and dusty phases are given in Eqs. (1) – (6).

Momentum exchange is modeled by a drag term proportional to the slip velocity (u_p-u) with momentum relaxation time τ_v. Thermal exchange is modeled by a temperature relaxation term proportional to (T_p-T) with thermal relaxation time τ_T.

The appropriate flow boundary requirements that have been enforced for hybrid nano- fluid and dust phases can be stated as follows:

$$\left.\begin{array}{ll} v=0,\ u=u_w(x),\ T=T_w & at\quad y=0 \\ u\to 0,\ \overline{u_p}\to 0,\ \overline{v_p}\to v,\ T\to T_\infty,\ \overline{T_p}\to T_\infty & as\quad y\to\infty \end{array}\right\} \tag{7}$$

Thermo-physical properties of hnf are:

$$A_1=\frac{\mu_{hnf}}{\mu_f},\ A_2=\frac{\rho_{hnf}}{\rho_f},\ A_3=\frac{\sigma_{hnf}}{\sigma_f},\ A_4=\frac{(\rho c_p)_{hnf}}{(\rho c_p)_f},\ A_5=\frac{k_{hnf}}{k_f} \tag{8}$$

$$\left.\begin{array}{l} A_1=\frac{1}{(1-\phi_1)^{2.5}(1-\phi_2)^{2.5}}, \\ \upsilon_{hnf}=\frac{\mu_{hnf}}{\rho_{hnf}},\quad \alpha_{hnf}=\frac{k_{hnf}}{(\rho c_p)_{hnf}} \\ A_2=\left\{(1-\phi_2)\left[(1-\phi_1)+\phi_1\left(\frac{\rho_{s_1}}{\rho_f}\right)\right]+\phi_2\frac{\rho_{s_2}}{\rho_f}\right\}, \\ A_3=\frac{\sigma_{s_2}+2\sigma_{nf}-2\phi_2(\sigma_{nf}-\sigma_{s_2})}{\sigma_{s_2}+2\sigma_{nf}+\phi_2(\sigma_{nf}-\sigma_{s_2})}\times\frac{\sigma_{s_1}+2\sigma_f-2\phi_1(\sigma_f-\sigma_{s_1})}{\sigma_{s_1}+2\sigma_f+\phi_1(\sigma_f-\sigma_{s_1})}, \\ A_4=(1-\phi_2)\left[(1-\phi_1)+\phi_1\left(\frac{(\rho c_p)_{s_1}}{(\rho c_p)_f}\right)\right]+\phi_2\frac{(\rho c_p)_{s_2}}{(\rho c_p)_f}, \\ A_5=\frac{k_{s_1}+2k_{bf}-2\phi_2(k_{bf}-k_{s_2})}{k_{s_2}+2k_{bf}+\phi_2(k_{bf}-k_{s_2})}\times\frac{k_{s_1}+2k_f-2\phi_1(k_f-k_{s_1})}{k_{s_1}+2k_f+\phi_1(k_f-k_{s_1})} \end{array}\right\} \tag{9}$$

Defining the similarity variables and transformations are:

$$u=rxf'(\eta),\quad v=-\sqrt{\upsilon_f r}f(\eta),\quad \eta=\sqrt{\frac{r}{\upsilon_f}}y,\ \theta(\eta)=\frac{T-T_\infty}{T_w-T_\infty}$$

$$\overline{u_p}=rxF_p'(\eta),\quad \overline{v_p}=-\sqrt{\upsilon_f r}F_p(\eta),\quad \theta_p(\eta)=\frac{\overline{T_p}-T_\infty}{T_w-T_\infty} \tag{10}$$

With the assistance of equations (8) – (10), equations (2) – (6) and their appropriate boundary conditions are transformed as given below.

Fluid Phase:

$$\frac{A_1}{A_2}f'''-(f')^2+ff''+\frac{1}{A_2}I^*\beta^*\left(F_p'-f'\right)-\frac{A_3}{A_2}Mf'-\frac{A_1}{A_2}Kf'-Fr(f')^2=0 \tag{11}$$

$$\left.\begin{array}{l} \left(A_5+\frac{4}{3}Rd\right)Pr\theta''+A_4Prf\theta'+PrI^*\beta_t\left(\theta_p-\theta\right)+ \\ \beta_v EcPr\left(F_p'-f'\right)^2+A_3MEc(f')^2=0 \end{array}\right\} \tag{12}$$

Dusty Phase:

$$\left(F_p'\right)^2-F_pF_p''-\beta^*\left(f'-F_p'\right)=0 \tag{13}$$

$$F_p\theta_p'+\gamma\beta_t\left(\theta-\theta_p\right)=0 \tag{14}$$

Corresponding boundary condition are

$$\left.\begin{array}{l} f'(\eta)=1,\ f(\eta)=0,\ \theta(\eta)=1,\qquad at\quad \eta=0, \\ \left.\begin{array}{l} f'(\eta)=0,\ F_p'(\eta)=0, \\ F_p(\eta)=f(\eta),\theta(\eta)=0, \\ \theta_p(\eta)=0 \end{array}\right\} as\quad \eta\to\infty. \end{array}\right\} \tag{15}$$

The dimensional form of *Cf* and *Nu*r are given by

$$C_f=\frac{\tau_w}{\rho_f u_w^2},Nu_r=-\left(k_{hnf}+\frac{16\ \sigma^*{T_\infty}^3}{3k^*}\right)\ \frac{r\left(\frac{\partial T}{\partial y}\right)_{y=0}}{k_f(T_w-T_\infty)} \tag{16}$$

where shear stress τ_w is

$$\tau_w=\mu_{hnf}\left.\frac{\partial u}{\partial y}\right|_{y=0} \tag{17}$$

The non-dimensional form of Eq. (16) is converted as

$$Re_r^{\frac{1}{2}}C_f=A_1f''(0), \tag{18}$$

$$(Re_r)^{-\frac{1}{2}}\ Nu_r=\ -\left(\frac{k_{hnf}}{k_f}+\frac{4}{3}Rd\right)\ \theta'(0) \tag{19}$$

where Re_r is the local Reynolds number.

Entropy generation analysis

$$\left.\begin{array}{l} S_{gen}'''=\frac{k_f}{T_\infty^2}\left[\frac{k_{hnf}}{k_f}+\frac{16\sigma^*T_\infty^3}{3k^*k_f}\right]\left(\frac{\partial T}{\partial z}\right)^2+ \\ \frac{\mu_{hnf}}{T_\infty}\left(\frac{\partial u}{\partial y}\right)^2+\left(\frac{\sigma_{hnf}B^2}{T_\infty}\right)u^2 \end{array}\right\} \tag{20}$$

The Entropy generation number N_G becomes

$$\left.\begin{aligned} N_G &= \frac{S'''_{gen}}{(k_f r\Delta T/T_W\upsilon_f)} \\ &= \alpha\left(A_5+\tfrac{4}{3}Rd\right)(\theta')^2 + A_3MBr(f')^2 \\ &+ A_1Br(f'')^2 \end{aligned}\right\} \tag{21}$$

The Bejan number is

$$Be = \frac{\alpha\left(A_5+\frac{4}{3}Rd\right)(\theta')^2}{\alpha\left(A_5+\frac{4}{3}Rd\right)(\theta')^2 + A_1Br\left(f''\right)^2 + A_3MBr\left(f'\right)^2} \tag{22}$$

The non-dimensional quantities are

$I^* = \frac{Nm}{\rho_f}$ is the dust particles with mass concentration,

$Br = \frac{\mu_f {u_w}^2}{k\Delta T}$ is the Brinkman number,

$\alpha = \frac{\Delta T}{T_w}$ is the temperature ratio parameter,

$\beta_v = \frac{1}{r\tau_v}$ is the fluid-particle interaction parameter,

$\gamma = \frac{(c_p)_f}{r_m}$ is the ratio of specific heat,

$Fr = \frac{C_F u_w}{\sqrt{k}}$ is the inertia coefficient,

$Rd = \frac{4\sigma^* T_\infty^3}{3k^* k_f}$ is the radiation parameter,

$Ec = \frac{(u_w)^2}{(c_p)_f (T_w - T_\infty)}$ is the Eckert number,

$\beta_t = \frac{1}{r\tau_T}$ is the fluid-particle interaction parameter for temperature,

$Pr = \frac{\mu_f (c_p)_f}{k_f}$ is the Prandtl number,

$\beta^* = \frac{K}{rm}$ is the particle interaction parameter,

$M = \frac{\sigma_f B^2}{r\rho_f}$ is the magnetic field parameter, and

$K = \frac{\upsilon_f}{rk^*}$ is the porosity parameter.

Tab. 1. The thermophysical characteristic of blood and ternary nanoparticles [26–28]

Property	Engine Oil	Cobalt	MWCNT
Density $\rho\ (kgm^{-3})$	863	8900	1600
Specific heat $C_p\ (Jkg^{-1}K^{-1})$	2048	420	796
Heat conductivity $k_f\ (Wm^{-1}K^{-1})$	0.1404	100	3000
Electrical conductivity $\sigma\ (\Omega m)^{-1}$	55×10^{-6}	1.602×10^{7}	1.9×10^{-4}

3. NUMERICAL METHOD

It is determined that the Bvp4c technique is the most effective approach for numerically solving the non-dimensional system of equations (10–14) and (15). With this technique, we begin by transforming the fundamental differential equations into a set of first-order ODEs as follows.

$$f = j_1, f' = j_2, f'' = j_3, f''' = j_3{}', \theta = j_4, \theta' = j_5, \theta'' = j_5{}', F = j_6,$$
$$F' = j_7, F'' = j_7{}', \theta_p = j_8, \theta_p{}' = j_8{}'$$

$$\begin{cases} j_1{}' = j_2 \\ j_2{}' = j_3 \\ j_3{}' = -\left[\dfrac{-(j_2)^2 + j_1j_3 + \frac{1}{A_2}I^*\beta^*(j_7 - j_2) - \frac{A_3}{A_2}Mj_2 - \frac{A_1}{A_2}Kj_2 - Fr(j_2)^2}{\frac{A_1}{A_2}}\right] \\ j_4{}' = j_5 \\ j_5{}' = -\left[\dfrac{PrA_4\, j_1j_5 + PrI^*\beta_t(j_8 - j_4) + \beta_v EcPr(j_7 - j_2)^2 + A_3MEc(j_2)^2}{\left(\frac{k_{hnf}}{k_f} + \frac{4}{3}Rd\right)Pr}\right] \\ j_6{}' = j_7 \\ j_7{}' = -\left[\dfrac{(j_7)^2 - \beta^*(j_2 - j_7)}{j_6}\right] \\ j_8{}' = j_9 \\ j_9{}' = -\left[\dfrac{\gamma\beta_t(j_4 - j_8)}{j_4}\right] \end{cases}$$

As well the boundary conditions are

$$\begin{cases} j_2(0) = 1, \\ j_1(0) = 0, \\ j_4(0) = 1, \\ j_2(\infty) = 0, \\ j_6(\infty) = j_1(\infty), \\ j_7(\infty) = 0, \\ j_4(\infty) = 0, \\ j_8(\infty) = 0. \end{cases}$$

The set of nonlinear ODEs was integrated using MATLAB's bvp4c routine with adaptive mesh refinement. The domain was truncated at η_{max}, where the velocity and temperature profiles reached their asymptotic values. The initial mesh contained 300 points, and the tolerance parameters were set to *RelTol* = 10^{-6} and *AbsTol* = 10^{-8}. The initial guess functions were selected as exponentially decaying profiles to match the boundary conditions at the wall and far-field. Convergence was verified by mesh refinement and domain extension, confirming the numerical accuracy within 0.05%.

Code Validation:

The results of the present code were compared to those obtained by Mishra et al. for the case of various values of Prandtl number, as shown in Table 2. We discovered a significant level of convergence between the current findings. In this case, the step size in the technique is $(h = 0.001)$, and the operation is frequent until the desired level (1×10^{-8}) of accuracy is reached. As a result, the current code is justified.

Tab. 2. Comparison of $-\theta'(0)$ for $\beta = \beta_T = Ec = \phi_1 = \phi_2 = \phi_p = 0$

Pr	Mishra et al.[23]	Present results (Bvp4c)
0.72	1.088623	1.088612
1	1.333333	1.333333
10	4.796819	4.796820

4. RESULTS AND DISCUSSION

The results of the comparison are acquired from Table 2, which displays the rate of heat transfer in the immediate area for a variety of Pr values. The findings of both investigations were determined to be quite accurate. The *M, K, Rd*, β_v, *Ec, Fr, Pr, I**,β_t, β^* all are given a physical explanation in this section. Each parameter is changed, while the others remain the same

$$M = 0.5,\ K = 0.2,\ \beta^* = 0.1,\ I^* = 0.1,$$

$$Fr = 0.2, Ec = 0.5, Re = 0.5, \alpha = 0.1, \beta_v = 0.3,$$

$$\beta_t = 0.2.$$

The nature of M against the $f'(\eta)$ profile and energy outline are seen in Figs 2 and 6. For the higher values of M the $f'(\eta)$ outline decreases. Physically, as the magnetic field M upsurges, it generates a Lorentz force, which slows the fluid flow. The Lorentz force acts in opposition to fluid motion, slowing it down and reducing the velocity field; nevertheless, we found the reverse tendency with respect to the temperature profile. A representation of the impact that the mass concentration has on the velocity outline may be seen in Fig. 3. For the higher values of the mass concentration the velocity profile decreases, while the same trend we noticed on the energy profile is seen in Fig 10. Fig. 4 shows that inertia coefficient on velocity profile. For the larger values of Fr, the velocity outline decreases for both hybrid and dusty cases. It is possible to see the impact that the porosity K has on the velocity outline in Fig. 5. The velocity of the nanofluid will decrease as the value of K increases towards higher levels. When the porosity parameter is raised, there is a corresponding increase in the amount of resistance that is created, which causes the flow of the liquids to be slowed down. The influence that the radiation generated on the energy profile may be observed in Fig. 7. The thermal profile will improve when the radiation parameter values increase. From a physical standpoint, related with the more temperature and the viscosity of the energy boundary layer. Fig 8 has an effect on the energy profile via its impact on the fluid interaction parameter. The fluid interaction parameter for both the hybrid case and the dusty scenario drops in value when larger values are applied, and this has an effect on the temperature profile. It can be obtained to see the impact that dusty and hybrid nanofluids have on the energy profile by referring to Fig. 9, which illustrates the impact for a number of different Eckert values. In terms of the physical world, the amount of additional kinetic energy that is deposited in the fluid particles that are brought into contact with the frictional heating system grows in a manner that is proportional to the Ec number. Because of these factors, the energy profile improves, which in turn leads to an increase in the values of the Ec number. Fig 11 demonstrates that the β_t parameter has an effect on the energy profile. For the larger values of β_t for temperature, the energy profile enhances. Physically, this is due to the existence of dust particles in the liquid, which cause friction and obstruct the flow. And also, the transport liquid declines thermal energy and kinetic energy upon contact with dust particles. Fig. 12 shows the effect of the $I^*\ and\ M$parameters on the $\mathrm{C_f}\ (\mathrm{Re})_\mathrm{r}^{0.5}$. It shows that the $\mathrm{C_f}\ (\mathrm{Re})_\mathrm{r}^{0.5}$is slowly cumulative in all circumstances of the larger values of Dust particles with mass concentration, while the decreasing tendency we observed on enlarging the M parameter values, On the contrary side, we noticed an opposite behaviour on the Nusselt number profile, which is shown in Fig.13. Fig 14 demonstrations the effect of the $Rd\ and\ M$parameters on the Nusselt number. When increasing the both parameters increased in Nusselt number profile, while the decreasing tendency we observed on minimum value 0.45. In cooling systems (like nuclear reactors or MHD generators), excessive magnetic or radiative effects can reduce heat removal efficiency.

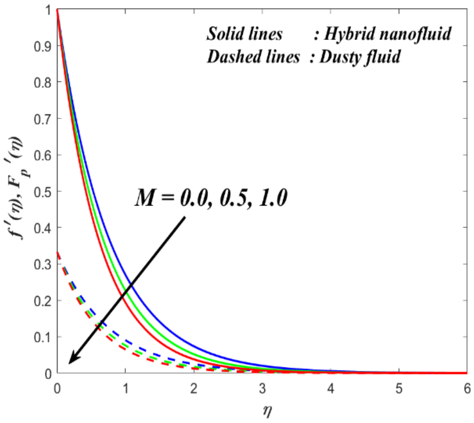

Fig. 2. Sway of Mon $f'(\eta), F_p'(\eta)$

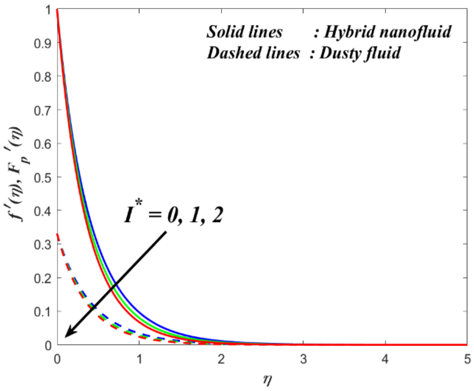

Fig. 3. Sway of I^*on $f'(\eta), F_p'(\eta)$

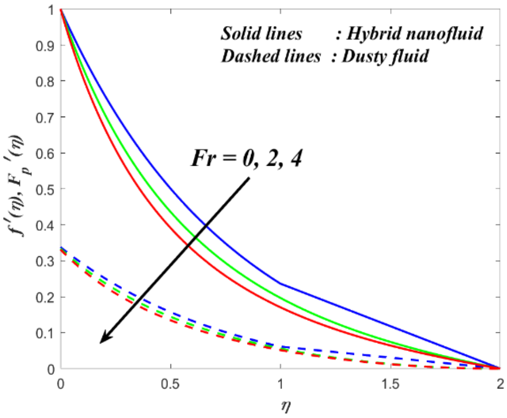

Fig. 4. Sway of Fron $f'(\eta), F_p'(\eta)$

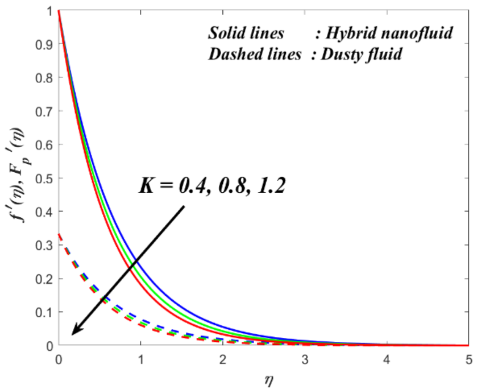

Fig. 5. Sway of Kon $f'(\eta), F_p'(\eta)$

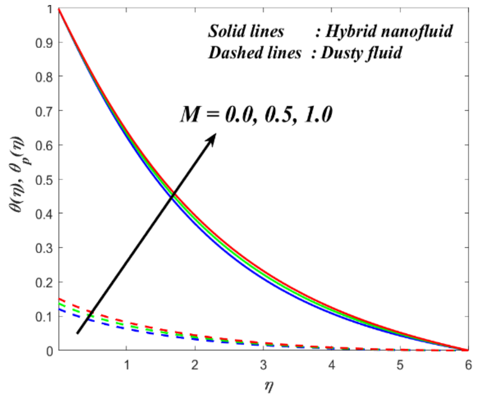

Fig. 6. Sway of Mon $\theta(\eta), \theta_p(\eta)$

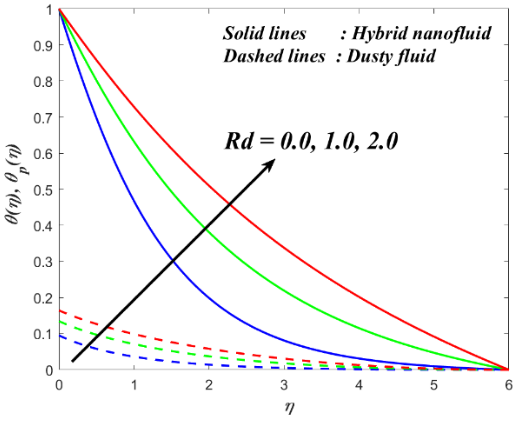

Fig. 7. Sway of Rdon $\theta(\eta), \theta_p(\eta)$

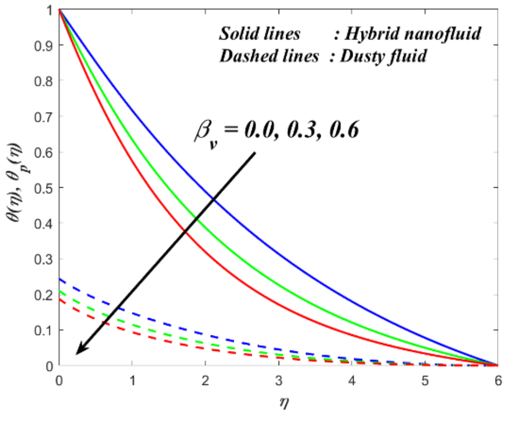

Fig. 8. Sway of $\beta_v$on $\theta(\eta), \theta_p(\eta)$

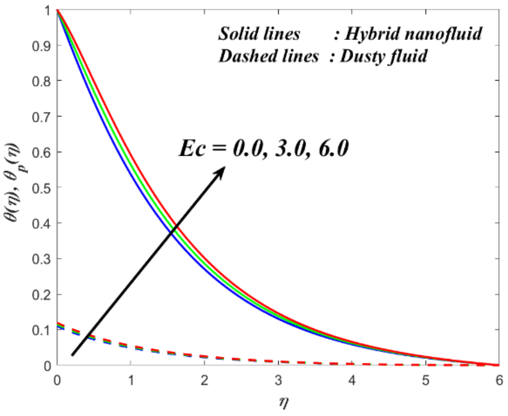

Fig. 9. Sway of Econ $\theta(\eta), \theta_p(\eta)$

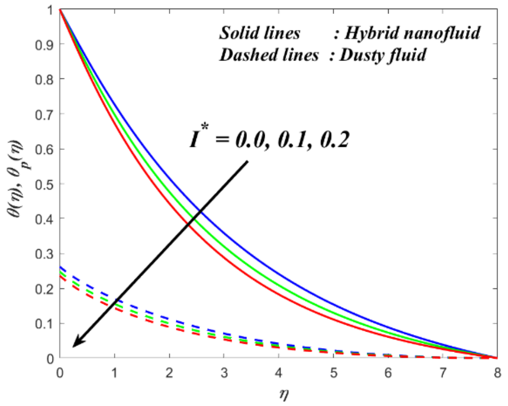

Fig. 10. Sway of I^*on $\theta(\eta), \theta_p(\eta)$

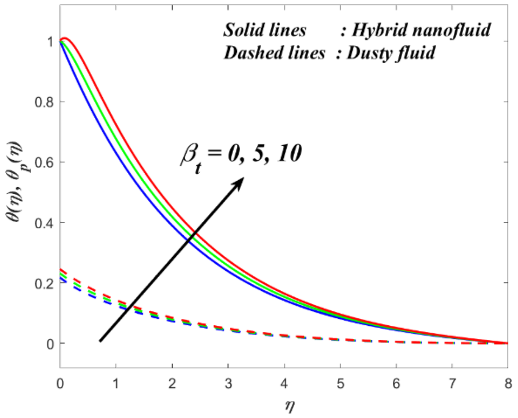

Fig. 11. Sway of$\beta_t$on $\theta(\eta), \theta_p(\eta)$

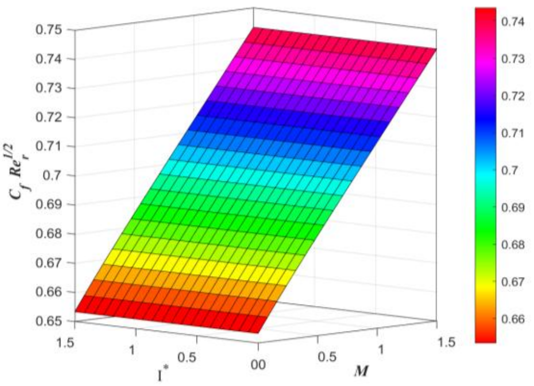

Fig. 12. Sway of $I^*$and$M$on$\mathrm{C_f}$ $(\mathrm{Re})_r^{0.5}$

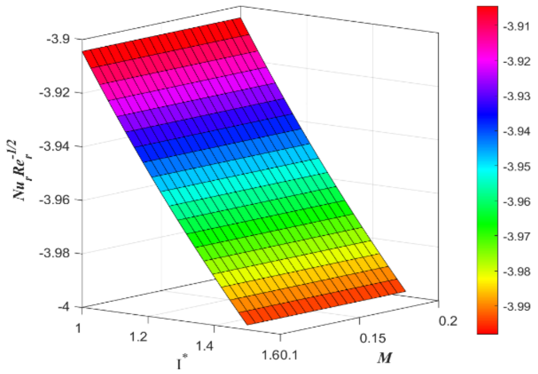

Fig. 13. Sway of $I^*$and$M$on$\mathrm{Nu_r}$ $(\mathrm{Re})_r^{-0.5}$

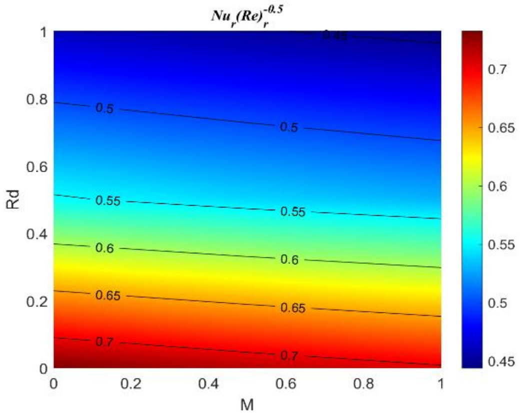

Fig. 14. Contour graph of $Rd$and$M$on$\mathrm{Nu_r}$ $(\mathrm{Re})_r^{-0.5}$

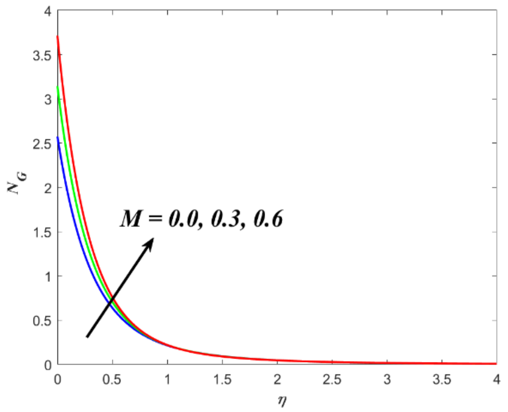

Fig. 15. Sway of Mon N_G

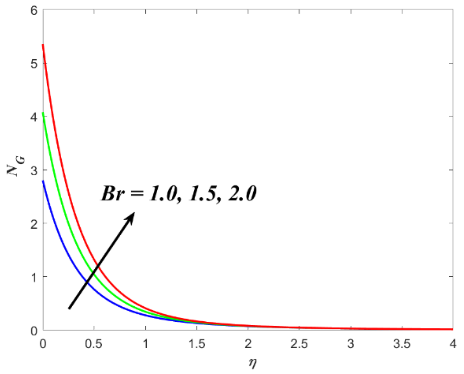

Fig. 16. Sway of Bron N_G

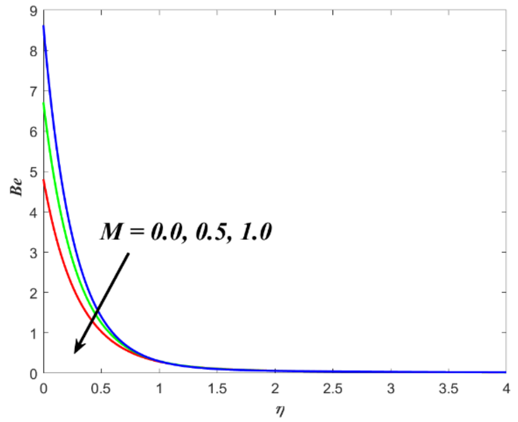

Fig. 17. Sway of M on Be

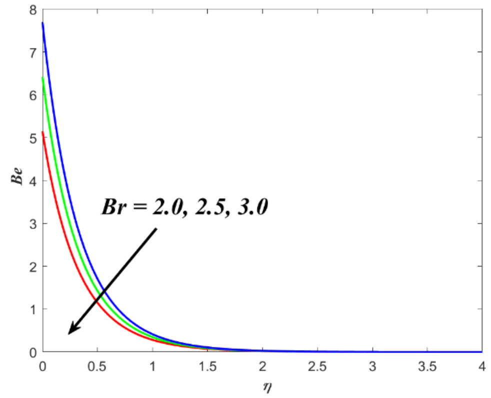

Fig. 18. Sway of Br on Be

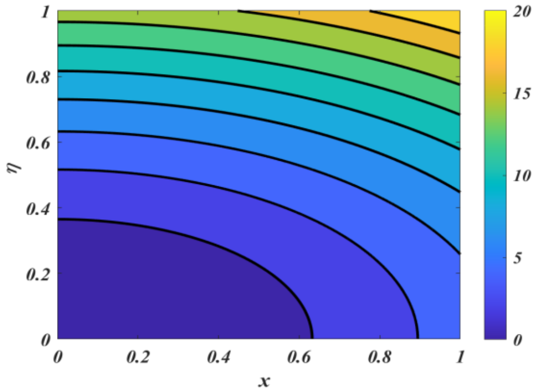

Fig. 19. Sway of $M = 1$ for Stream lines

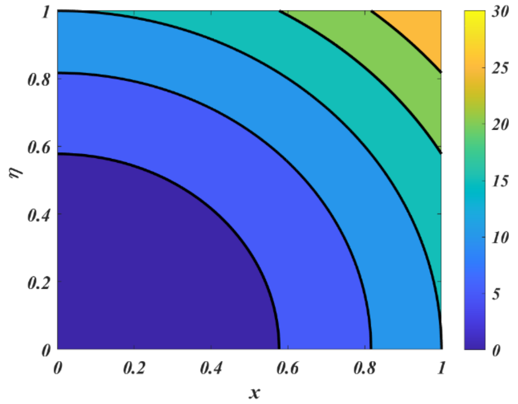

Fig. 20. Sway of $M = 2$ for Stream lines

Fig. 15 shows the effect that the M parameter has on the contour of the entropy generation. The entropy generation profile improves as the values of M are increased to higher concentrations. From a strictly physical point of view, a rise in M results in an increase in the rate at which entropy is formed. This is because of the high friction that is induced by the higher Lorentz force. On the other hand, we observed the opposite behavior on the Be profile, which is seen in Fig. 17. Fig 16 demonstrates that the rate of entropy generation outline increases for increasing Br values. This scenario in the results of the entropy production rate is due to the strengthening of viscous effects with the rise in the Brinkman number, although the contradictory nature we detected on the Bejan number profile which is presented in Fig 18. Figs 19 and 20 demonstrations the M=1, 2 influences on streamlines. Magnetic parameter strength draws electrical conductivity molecules more towards the top. When M is small, the magnetic field is weaker, so the Lorentz force (the resistive electromagnetic force) acting on the conducting fluid is limited. As a result, the flow remains energetic and faster, and convective transport dominates.

5. CONCLUSION

A numerical solution for MHD flow on Dar-cy-Forchheimer flow on a stretched sheet was investigated in the previous research project that was being conducted. The problem of velocity and temperature was solved by using the numeri-cal approach, which is known as Bvp4c. The re-sult was a solution that was actually applicable to the model. The purpose of this kind of research is to an aircraft engine has a number of duties that are performed by engine oil. These functions in-clude lubrication, cooling, maintenance, prevent-ing corrosion, and reducing noise. Lubrication is the matter of utmost significance. In the absence of lubrication, it is the natural course of events that all moving parts would quickly escape. The findings are displayed in a number of different graphical styles, such as streamlines, surface plots in three dimensions, and a two-dimensional plot. The research produced a number of interesting findings, which are listed below:

- Increasing levels of the magnetic field and porosity parameter cause a reduction in the velocity outline.
- In the process of enhancing the radiation parameter, the temperature profile saw a significant improvement.
- The skin friction factor slowly increased for the larger values of the parameter.
- The Nu profile enhances, for the increasing values of the Rd.
- Streamlines have an oscillating character, which is necessary for magnifying the magnetic field parameter.

REFERENCES

1. Nabwey HA, Mahdy A. Transient flow of micropolar dusty hybrid nanofluid loaded with Fe3O4-Ag nanoparticles through a porous stretching sheet. Results in Physics. 2021 Feb 1;21:103777. https://doi.org/10.1016/j.rinp.2020.103777
2. Jakeer S, Reddy PB. Entropy generation on the variable magnetic field and magnetohydrodynam-ic stagnation point flow of Eyring–Powell hybrid dusty nanofluid: Solar thermal application. Pro-ceedings of the Institution of Mechanical Engi-neers, Part C: Journal of Mechanical Engineering Science. 2022 Jul;236(13):7442-55. https://doi.org/10.1177/09544062211072457
3. Divya A, Bala Anki Reddy P. Aerospace aspects of electromagnetohydrodynamic dusty flow of hybrid nanofluid with entropy generation over a rotating disk. Proceedings of the Institution of Mechanical Engineers, Part E: Journal of Process Mechanical Engineering. 2023 Apr;237(2):196-206. https://doi.org/10.1177/09544089221102417
4. Saffman PG. On the stability of laminar flow of a dusty gas. Journal of fluid mechanics. 1962 May;13(1):120-8. https://doi.org/10.1017/S0022112062000555
5. Marble FE. Dynamics of dusty gases. Annual Review of Fluid Mechanics. 1970 Jan 1;2(1):397-446. https://doi.org/10.1146/annurev.fl.02.010170.002145
6. Jakeer S, Reddy PB, Rashad AM, Nabwey HA. Impact of heated obstacle position on magneto-hybrid nanofluid flow in a lid-driven porous cavi-ty with Cattaneo-Christov heat flux pattern. Al-exandria Engineering Journal. 2021 Feb 1;60(1):821-35. https://doi.org/10.1016/j.aej.2020.10.011
7. Jana S, Salehi-Khojin A, Zhong WH. Enhance-ment of fluid thermal conductivity by the addi-tion of single and hybrid nano-additives. Thermo-chimica acta. 2007 Oct 15;462(1-2):45-55. https://doi.org/10.1016/j.tca.2007.06.009
8. Hussain M, Hanif Z, Hussain M, Amer I, Man-soor M. Nonlinear radiative MHD flow of ternary nanofluid with Darcy–Forchheimer porous media: entropy generation analysis. Journal of Thermal Analysis and Calorimetry. 2025 Jan 6:1-25. https://doi.org/10.1007/S10973-024-13785-2
9. Hussain M, Rasool M, Hussain M, Mansoor M, Amer I, Hanif Z. Impact of Joule Heating and Magnetic Field on Heat Transfer of Shape-Dependent Ternary Nanofluid Past Through Po-rous Stretching Sheet. Journal of Nanofluids. 2025 Feb 1;14(1):118-27. https://doi.org/10.1166/JON.2025.2221
10. Divya A, Reddy PB. Electromagnetohydrody-namic unsteady flow with entropy generation and hall current of hybrid nanofluid over a rotating disk: an application in hyperthermia therapeutic aspects. Proceedings of the Institution of Me-chanical Engineers, Part C: Journal of Mechanical Engineering Science. 2022 Jul;236(13):7511-28. https://doi.org/10.1177/09544062221076294
11. Chamkha AJ, Dogonchi AS, Ganji DD. Magne-to-hydrodynamic flow and heat transfer of a hy-brid nanofluid in a rotating system among two surfaces in the presence of thermal radiation and Joule heating. Aip Advances. 2019 Feb 1;9(2). https://doi.org/10.1063/1.5086247
12. Shaw S, Samantaray SS, Misra A, Nayak MK, Makinde OD. Hydromagnetic flow and thermal interpretations of Cross hybrid nanofluid influ-enced by linear, nonlinear and quadratic thermal radiations for any Prandtl number. International Communications in Heat and Mass Transfer. 2022 Jan 1;130:105816. https://doi.org/10.1016/j.icheatmasstransfer.2021.105816
13. Jakeer S, Reddy SR. Electrokinetic membrane pumping flow of hybrid nanofluid in a vertical microtube with heat source/sink effect. The European Physical Journal Plus. 2023 Jun 2;138(6):489. https://doi.org/10.1140/epjp/s13360-023-04118-7
14. Awais M, Bibi M, Ali A. Numerical treatment for MHD axisymmetric rotating Bodewadt rheology under Ohmic heating and viscous dissipation effects. https://doi.org/10.21203/rs.3.rs-1364435/v1
15. Reddy SR, Reddy PB. Thermal radiation effect on unsteady three-dimensional MHD flow of micropolar fluid over a horizontal surface of a parabola of revolution. Propulsion and Power Research. 2022 Mar 1;11(1):129-42. https://doi.org/10.1016/j.jppr.2022.01.001
16. Bhatti MM, Arain MB, Zeeshan A, Ellahi R, Do-ranehgard MH. Swimming of Gyrotactic Micro-organism in MHD Williamson nanofluid flow between rotating circular plates embedded in po-rous medium: Application of thermal energy stor-age. Journal of Energy Storage. 2022 Jan 1;45:103511. https://doi.org/10.1016/j.est.2021.103511
17. Sajid T, Algarni S, Ahmad H, Alqahtani T, Jam-shed W, Eid MR, Irshad K, Amjad A. Explora-tion of irreversibility process and thermal energy of a tetra hybrid radiative binary nanofluid focus-ing on solar implementations. Nanotechnology Reviews. 2024 Jul 4;13(1):20240040. https://doi.org/10.1515/ntrev-2024-0040

18. Sakkaravarthi K, Reddy PB, Sakthi I. Entropy optimization in Casson tetra-hybrid nanofluid flow over a rotating disk with nonlinear thermal radiation: A Levenberg–Marquardt neural net-work approach. Journal of Computational Design and Engineering. 2024 Oct;11(5):333-54. https://doi.org/10.1093/jcde/qwae086
19. Hussain M, Ali A, Ranjha QA, Ahmad I, Anwar MS. Radiative magneto-cross Eyring-Powell flow with activation energy past porous stretching wedge considering suction/injection and ohmic heating effect. Numerical Heat Transfer, Part B: Fundamentals. 2024 Jul 2;85(7):867-82. https://doi.org/10.1080/10407790.2023.2257383
20. Ali A, Ali M, Hussain M, Ali I, Fenta A. The in-fluence of thermophoresis and Brownian motion on maxwell nanofluids utilizing Cattaneo-Christov double diffusion theory. Advances in Mechanical Engineering. 2024 Nov;16(11):16878132241302999. https://doi.org/10.1177/16878132241302999
21. Anwar MS, Irfan M, Muhammad T, Hussain M. Flow analysis of Williamson model over a moving surface with nonlinear convection/diffusion and variable thermal conductivity. Numerical Heat Transfer, Part A: Applications. 2025 Oct 2;86(19):6737-54. https://doi.org/10.1080/10407782.2024.2345587
22. Mishra SR, Khan MI, Rout BC. Dynamics of dust particles in a conducting dusty nanomateri-als: A computational approach. International Communications in Heat and Mass Transfer. 2020 Dec 1;119:104967. https://doi.org/10.1016/j.icheatmasstransfer.2020.104967
23. Reddy MG, Rani MS, Kumar KG, Prasanna-kumar BC, Lokesh HJ. Hybrid dusty fluid flow through a Cattaneo–Christov heat flux model. Physica A: Statistical Mechanics and its Applica-tions. 2020 Aug 1;551:123975. https://doi.org/10.1016/j.physa.2019.123975
24. Parida SK, Mishra S, Dash RK, Pattnaik PK, Khan MI, Chu YM, Shah F. Dynamics of dust particles in a conducting water-based kerosene nanomaterials: a computational approach. Interna-tional Journal of Chemical Reactor Engineering. 2021 Aug 17;19(8):787-97. https://doi.org/10.1515/ijcre-2020-0204
25. Divya A, Bala Anki Reddy P. Aerospace aspects of electromagnetohydrodynamic dusty flow of hybrid nanofluid with entropy generation over a rotating disk. Proceedings of the Institution of Mechanical Engineers, Part E: Journal of Process Mechanical Engineering. 2023 Apr;237(2):196-206.https://doi.org/10.1177/09544089221102417
26. Mourad A, Aissa A, Abed AM, Toghraie D, Ak-bari OA, Guedri K, Younis O, Marzouki R. MHD natural convection of Fe3O4-MWCNT/Water hybrid nanofluid filled in a porous annulus be-tween a circular cylinder and Koch snowflake. Alexandria Engineering Journal. 2023 Feb 15;65:367-82.https://doi.org/10.1016/j.aej.2022.09.035
27. Ahmad S, Nadeem S, Muhammad N, Issakhov A. Radiative SWCNT and MWCNT nanofluid flow of Falkner–Skan problem with double strati-fication. Physica A: Statistical Mechanics and its Applications. 2020 Jun 1;547:124054. https://doi.org/10.1016/J.PHYSA.2019.124054

Gunisetty Ramasekhar: https://orcid.org/0000-0002-3256-3145

Shaik Jakeer: https://orcid.org/0000-0002-6350-1457

S. R. R. Reddy: https://orcid.org/0000-0001-5501-570X

P. Vijay Kumar: https://orcid.org/0000-0003-0450-3732

P. Durgaprasad: https://orcid.org/0000-0002-1753-7088